

pubs.acs.org/ac Article

Pulse-Picking Multimodal Nonlinear Optical Microscopy

Matthew G. Clark, Gil A. Gonzalez, and Chi Zhang*



Cite This: Anal. Chem. 2022, 94, 15405-15414



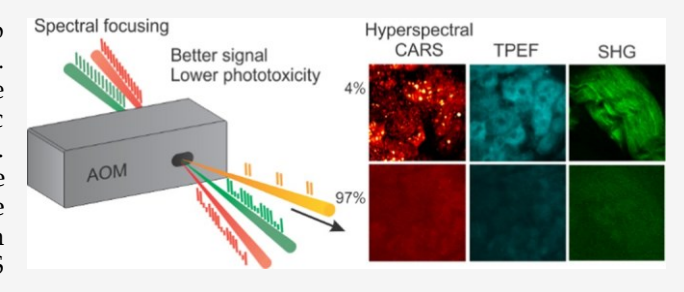
ACCESS

III Metrics & More

Article Recommendations

Supporting Information

ABSTRACT: Nonlinear optical microscopy techniques can map chemical compositions in biological samples in a label-free manner. Commonly used nonlinear optical processes for imaging include multiphoton excitation fluorescence (MPEF), second harmonic generation (SHG), and coherent Raman scattering (CRS). Femtosecond lasers are typically used for MPEF and SHG due to the requirement of high peak power for excitation, while picosecond lasers are preferred for CRS due to the need for high spectral resolution. Therefore, it is challenging to integrate CRS with MPEF and SHG for chemical imaging. We develop a pulse-



picking strategy based on an acousto-optic modulator that can program the duty cycle of the laser pulse train, significantly increasing the pulse peak power at low input average power. This approach offers strong enhancement of nonlinear optical signals and makes hyperspectral coherent anti-Stokes Raman scattering (CARS) microscopy compatible with MPEF and SHG for multimodal imaging at low laser average power. The pulse-picking method also enables the evaluation and comparison of phototoxicity of laser pulses at different average and peak power levels. The photo-perturbations to biological samples are evaluated using cellular dynamics and sample morphological changes, allowing the selection of optimal laser power for the best sensitivity and minimal phototoxicity.

INTRODUCTION

Chemical analysis of biological samples is the key to understanding biofunctions and diagnosing pathological transitions. There is a growing interest in the label-free acquisition of chemical information in living samples. Nonlinear optical microscopy techniques allow label-free mapping of chemicals with high resolution and speed. The commonly used nonlinear optical processes for imaging include multiphoton excitation fluorescence (MPEF), second harmonic generation (SHG), and coherent Raman scattering (CRS). MPEF is sensitive to probing intrinsic fluorophores such as nicotinamide adenine dinucleotide hydrogen (NADH) and flavin adenine dinucleotide (FAD). 1,2 SHG is selective to noncentrosymmetric compositions such as collagen and elastin.^{3,4} CRS processes, including both coherent anti-Stokes Raman scattering (CARS) and stimulated Raman scattering (SRS), harness molecular vibrational transitions excited by ultrafast laser pulses for chemical analysis.^{5–8} These modalities can be integrated into a single laser-scanning microscope for multimodal imaging.9-12 In general, MPEF and SHG use femtosecond (fs) laser pulses for signal excitation. 13-17 CRS, however, prefers picosecond (ps) laser pulses to achieve high spectral resolution. 18,19 Hyperspectral CRS microscopy applies either two narrow-band ps laser pulses, combined narrow and broadband laser pulses, or spectrally chirped broadband laser pulses.^{20–28} The different requirement makes hyperspectral CRS less compatible with MPEF and SHG. It is necessary to develop effective ways to better integrate these imaging modalities without increasing laser phototoxicity.

One approach is to use lasers with lower repetition rates and higher pulse energy, which gives higher peak power at the same average power.^{29–32} A tunable repetition rate would provide better flexibility for different imaging requirements. One way to reduce the repetition rate is using Pockels cells. The Xie group applied Pockels cells to reduce 80 MHz synchronized ps lasers to 8 MHz for single-color CARS imaging.³³ The Cheng group has demonstrated using Pockels cells as a tunable pulse picker for single-color CARS imaging with high-repetition rate ps lasers.^{34,35} However, a separate fs laser was used for MPEF and SHG imaging.³⁵ In addition, Pockels cells require very high voltage (5000 V) power supplies and signal amplifiers to operate.

In this work, we deploy a pulse-picking approach based on an acousto-optic modulator (AOM) for simultaneous MPEF, SHG, and hyperspectral CARS imaging. Applying one of the laser beams at the Bragg angle error condition, the pump and Stokes beams at the 1st order of the AOM can be collinearly combined. This pulse-picking nonlinear optical microscope allows flexible control of the optimal number of pulses at each pixel to maximize sensitivity and minimize photo-perturbation to biological samples. It also enables the integration of

Received: July 28, 2022 Accepted: October 10, 2022 Published: October 25, 2022





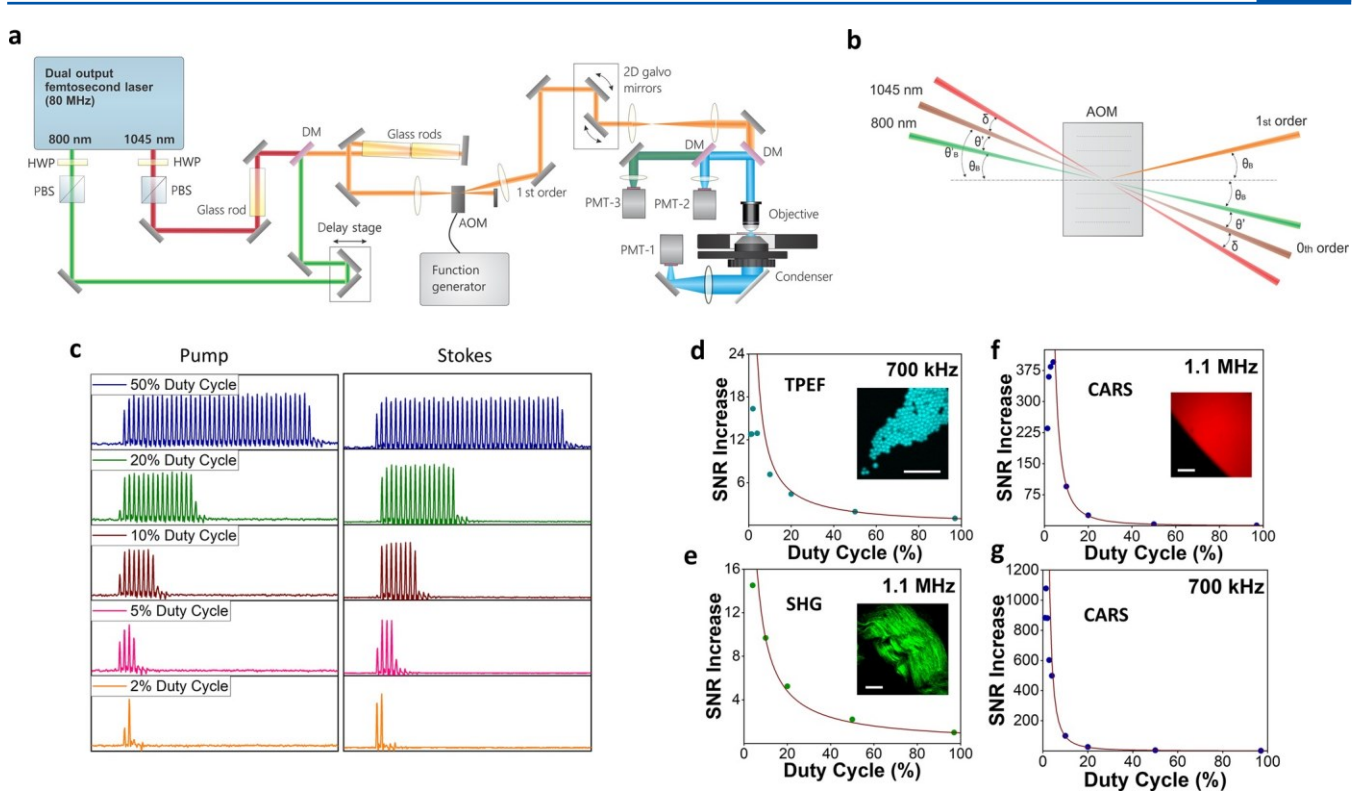


Figure 1. Pulse-picking technology for sensitivity improvement of TPEF, SHG, and CARS modalities. (a) Schematic of the pulse-picking multimodal nonlinear optical microscope. PBS, polarization beam splitter; AOM, acousto-optic modulator; PMT, photomultiplier tube; DM, dichroic mirror; HWP, half-wave plate. (b) Schematic of spatial overlapping of pump and Stokes beams at the 1st-order diffraction of an AOM. (c) Pump and Stokes pulse trains from the AOM 1st order beam at 50, 20, 10, 5, and 2% duty cycles. (d) TPEF SNR increases versus duty cycle at 0.7 MHz modulation frequency. Dots are experimental data, curves are the theoretical function of 1/D, and D is the duty cycle. The image inset shows a TPEF image of fluorescent microparticles from which SNR values were derived. (e) SHG SNR increases at 1.1 MHz modulation frequency at different duty cycles. Dots are experimental data; the curve is the theoretical function of 1/D. The image inset shows a mouse tail tendon specimen from which SNR values were derived. (f) CARS SNR increases versus duty cycle at 1.1 MHz modulation frequency. Dots are experimental data; the curve is the theoretical function of $1/D^2$. The image inset shows the edge of a sample of DMSO from which SNR values were derived. (g) CARS SNR increases versus duty cycle at 0.7 MHz modulation frequency. Scale bars, $10 \, \mu m$.

hyperspectral CARS, MPEF, and SHG modalities using the same laser source. By adopting spectral focusing, we achieve high spectral resolution for hyperspectral CARS and good sensitivity for MPEF and SHG. In addition, the pulse-picking method allows evaluation of the phototoxicity of laser pulses at different average and peak power levels and optimization of laser pulses for multimodal CARS, MPEF, and SHG imaging. Using intact tissue and live cells, we evaluate the average and peak power ranges to minimize thermal and multiphoton-absorption-induced photodamage. Intercellular organelle dynamics are applied as a more sensitive way to quantify the photo-perturbation of high-energy pulses to live cells.

RESULTS AND DISCUSSION

Design of the Pulse-Picking Nonlinear Optical Microscope. To date, the most widely used light sources for nonlinear optical microscopy are high-repetition rate fs or ps lasers. Assuming an 80 MHz laser repetition rate and a 10 μ s pixel dwell time, there are 800 pulses on each image pixel. Since nonlinear optical signals are usually proportional to the square or cubic of laser peak power, reducing the number of pulses at each pixel with higher pulse energy can largely improve the sensitivity while maintaining the same average input power. The pulse-picking nonlinear optical microscopy system reported here is based on acousto-optics and can simultaneously work for two laser wavelengths. This system

integrates MPEF, SHG, and hyperspectral CARS modalities. The design of our microscope is illustrated in Figure 1a. A fs laser with synchronized dual outputs: one as the Stokes beam with a fixed wavelength at 1045 nm and the other as the pump beam with a tunable wavelength from 690 to 1300 nm. The two beams are combined and chirped by multiple SF-57 glass rods for spectral focusing.²¹ Before the microscope, the Stokes pulse is chirped to 1.8 ps while the pump pulse is chirped to 3.4 ps. The two pulses have the same chirp rate to ensure the best spectral resolution.^{21,23} The combined beams are sent to an AOM that is controlled by a function generator. Square waves with tunable duty cycles from 1.4 to 97% at various modulation frequencies are sent to the AOM for pulse-picking. We direct the 1st order AOM output to a lab-designed upright laser-scanning microscope with two photomultiplier tubes (PMTs) in the epi-direction and one in the forward direction. As shown in Figure 1a, we use PMT1 for forward-CARS (FCARS) detection, PMT2 for the acquisition of two-photon excitation fluorescence (TPEF) signals at 450 nm, and PMT3 for the collection of TPEF signals at 570 nm, SHG signals, or epi-CARS (ECARS) signals. A more detailed description of our experimental setup can be found in the Supporting Information.

We choose the 1st-order diffraction beam from the AOM over the 0th order for imaging since it has zero power at the "time-off" periods. This maximizes the nonlinear optical signal

generation at a fixed input average power. However, the AOM Bragg angles for the pump and Stokes wavelengths are different. To ensure beam overlap along the 1st order of diffraction, one of the beams needs to be slightly misaligned from the perfect Bragg angle. The AOM beam separation angle between the 0th and 1st orders is

$$\theta = \lambda f / V \tag{1}$$

where λ is the beam wavelength, f is the acoustic frequency, and V is the acoustic velocity. The Bragg angle is half of the separation angle

$$\theta_{\rm B} = \lambda f / (2V) \tag{2}$$

The laser beam geometry at the AOM for spatially overlapping pump and Stokes beams along the 1st order diffraction is illustrated in Figure 1b. We first let the pump beam at 800 nm enter the AOM at the Bragg angle $\theta_{\rm B}$. Both the 0th and the 1st order diffraction orders of this wavelength have an angle of $\theta_{\rm B}$ to the crystal surface normal. Assuming the Stokes beam at 1045 nm has a Bragg angle $\theta'_{\rm B}=\theta_{\rm B}+\theta'$, the incidence angle of this beam needs to be slightly detuned from $\theta'_{\rm B}$ to generate the 1st order diffraction in the same direction as

the 1st order pump beam. Let δ be the angle between the incidence angle and the Bragg angle of the Stokes beam. It satisfies

$$\theta_{B, \text{ Stokes}} = 2(\theta_{B} + \theta') = 2\theta_{B} + \theta' + \delta$$
 (3)

This gives $\delta = \theta'$, and indicates that when the pump and Stokes beams are collinear at the 1st order of pump, the angle between the incidence and the Bragg angle of the Stokes beam equals the angle difference between the pump and Stokes Bragg angles. In our optical configuration, $\delta = 0.39^{\circ}$. Our AOM driver has a center frequency of 200 MHz. If the center frequency is reduced to 80 MHz, δ is reduced to 0.15°. Using two mirrors in the Stokes-only beam path, we can fine-tune the incidence angle of the Stokes beam at the AOM to satisfy this condition. Using this method, we can reach a 60% efficiency for the pump and 42% efficiency for the Stokes beam using a 90% duty cycle. The loss of efficiency is due to the nonoptimal crystal anti-reflective coating and Bragg angle errors. If the wavelength of the pump beam is tuned from 800 nm (corresponding to 2930 cm⁻¹) to 890 nm (corresponding to 1667 cm⁻¹), the Bragg angle changes 0.14° at 200 MHz center frequency. Slight optimization of the pump beam might be needed to maximize CARS signals after far wavelength tuning.

Pulse-Picking for Sensitivity Improvement at the Same Average Input Power. Laser pulses from both the pump and Stokes beams picked by the AOM at different duty cycle values are displayed in Figure 1c. We estimate the rise time of the AOM in our experiment is ~23 ns for the Stokes and ~17 ns for the pump (see the Supporting Information), slightly longer than the time interval between adjacent pulses from the laser, which can also be inferred from Figure 1c. At high duty cycles, the number of pulses picked by the AOM is proportional to the duty cycle. At 5% duty cycle, we were able to pick 4 major pulses for both pump and Stokes beams at 1.1 MHz modulation frequency. When the duty cycle is reduced to 2% or below, as few as one major pulse can be picked.

Reducing the laser duty cycle would enhance the sensitivity of nonlinear optical microscopy at the same input average power. The intensity of the TPEF, SHG, and CARS signals can be expressed as

$$I_{\text{TPEF}}, I_{\text{SHG}} \propto I_{\text{p}}^2$$
 (4)

$$I_{\text{CARS}} \propto |\chi|^{(3)}|^2 I_{\text{p}}^2 I_{\text{s}} \tag{5}$$

where I_{CARS} , I_{p} , and I_{s} are, respectively, the intensities of the CARS, pump, and Stokes beams. Here, we are considering the SHG and TPEF signals generated only from the pump beam. $\chi^{(3)}$ is the third-order nonlinear optical susceptibility. The intensity of a laser pulse can be expressed as

intensity of a laser pulse can be expressed as
$$I = \underbrace{\frac{\varepsilon}{\tau A}} = \frac{P}{f\tau A}$$
(6)

Here, E, τ , and A are pulse energy, pulse width, and laser focus area of the laser beam, respectively, while P and f are the laser average power and repetition rate, respectively. By modulating combined laser beams at a lower frequency and applying a duty cycle of D, we have

$$\begin{split} P_{\text{TPEF}}\left(\text{or } P_{\text{SHG}}\right) &= fD_{\tau_{\text{TEPF}}}A \cdot I_{\text{TEPF}} \propto fD\tau_{\text{TPEF}}A \cdot I_{\text{p}}^{2} \\ &= fD_{\tau_{\text{TPEF}}}A \cdot \frac{\mathbf{j}}{\mathbf{j}} \frac{P_{\text{p}}}{D_{\text{p}}A} \frac{\mathbf{y}}{\mathbf{z}} \frac{1}{D} \\ &\mathbf{k} \mathbf{k} \mathbf{j} \frac{P_{\text{p}}}{\mathbf{k}} \mathbf{y} \mathbf{z} \frac{1}{D} \end{split} \tag{7}$$

$$\begin{split} P_{\text{CARS}} &= f D_{\text{t}} \text{CARS}^{A \cdot I} \text{CARS} \propto f D_{\text{t}} \text{CARS}^{A \cdot I} / \chi^{(3)} |^{2} \begin{cases} \frac{\mathbf{j}}{f} & P^{\mathbf{j}} & \mathbf{j}^{2} \\ \frac{\mathbf{j}}{f} D_{\text{t}} P^{A} & \mathbf{j}^{2} \end{cases} & f^{\mathbf{j}} \\ &= |\chi^{(3)}|^{2} \frac{P^{2} P}{f^{2} D^{2} A^{2}} \frac{\tau_{\text{CARS}}^{2}}{\tau_{p}^{2} \tau_{\text{s}}} \propto \frac{1}{D^{2}} \end{split} \tag{8}$$

These indicate the pulse-picking average signals of TPEF and SHG are proportional to the reciprocal of the duty cycle, while the pulse-picking CARS average signal is reciprocal to the square of the duty cycle.

To evaluate the signal-to-noise ratio (SNR) increase at the same average input power, we use fluorescent polystyrene beads and measure the fluorescence signal at 450 nm excited by 800 nm laser pulses (Figure 1d). For each duty cycle, the SNR is divided by the SNR of the 97% duty cycle to calculate the sensitivity increase. A 1/D curve is plotted as a reference. The TPEF SNR increase shows a near 1/D relation at high duty cycles and starts to deviate from the theoretical curve at lower duty cycles. We can obtain a 16.3 sensitivity increase at a 2% duty cycle, 0.7 MHz modulation. SHG signal improvement, which shows a similar dependence as the TPEF, was measured using a mouse tail tendon specimen and 1045/522 nm excitation/detection (Figure 1e). A sensitivity increase of 14.5 is achieved at a 2% duty cycle, 1.1 MHz modulation. Plots of TPEF/SHG SNR improvement versus duty cycle at other modulation frequencies are plotted in Figure S2, showing the maximum sensitivity enhancement of ~20 fold for both TPEF and SHG. We use the dimethyl sulfoxide (DMSO) CH₃ symmetric stretching peak at 2915 cm⁻¹ for CARS SNR analysis. A boundary of a DMSO drop sandwiched between two glass coverslips is imaged for SNR calculation. We measure the SNR of the DMSO by dividing the average value of the DMSO signal by the standard deviation of the empty area. The experimental data match the theoretical $1/D^2$ curve very well at high duty cycles but start to deviate from the theory at very low duty cycles (Figure 1f,g). The maximum sensitivity enhancement we can obtain is 1078 at 1.4% duty cycle, 0.7 MHz modulation (Figure 1g). The major cause of the sensitivity drop at very low duty cycles might be the unlocked phase

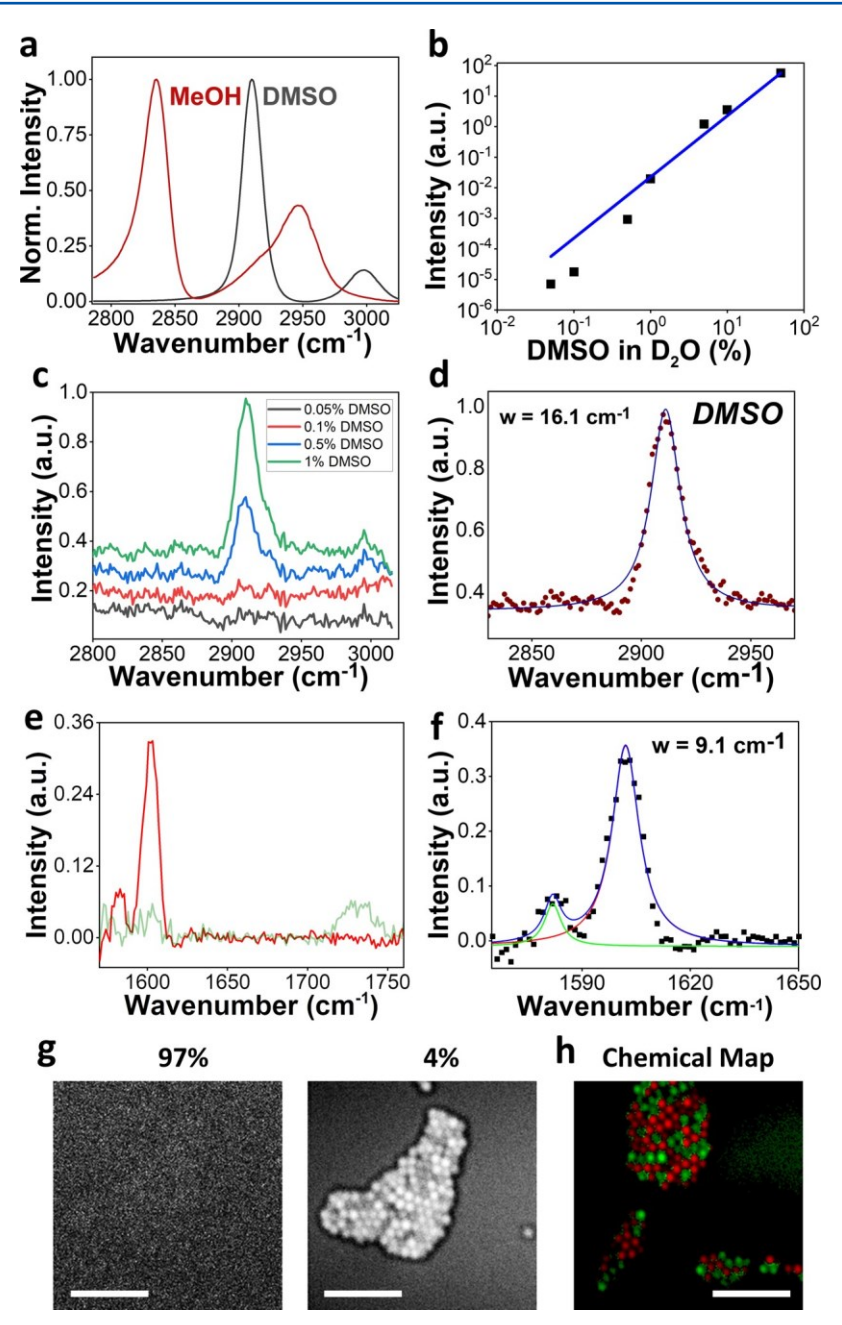


Figure 2. Characterizations of the pulse-picking nonlinear optical microscope. (a) CARS spectra of methanol and DMSO in the C–H region. (b) A plot of CARS signal intensity versus DMSO concentration (%) in D₂O. Dots are experimental values; the curve is the quadratic fitting of experimental results. (c) Phase-retrieved Raman spectra of 1–0.05% DMSO in D₂O. (d) Peak fitting of phase-retrieved Raman spectrum of 1% DMSO in D₂O. (e) Retrieved Raman spectra of 1 μm PS (red) and PMMA beads (green) in the fingerprint region. (f) Spectral peak fitting of PS 1583 and 1602 cm⁻¹ stretching. (g) CARS images of a mixture of 1 μm PS and PMMA beads at 97 and 4% duty cycles at the same input average power, 0.7 MHz modulation frequency. (h) Spectral phasor-generated chemical map of mixed beads (PS: red; PMMA: green) using the fingerprint hyperspectral CARS images. Power at the samples: 5.2 mW pump and 6.2 mW Stokes for the C–H imaging; 13.7 mW pump and 6.2 mW Stokes for the fingerprint imaging. Pixel dwell time: 10 μs. Scale bars, 10 μm.

between the function generator modulation and the laser pulse train. Frequency drifts between the two are less significant when the duty cycle is high since almost the same number of pulses can always be picked at any phase difference. However, when the duty cycle becomes low, especially below 4%, the phase drift can greatly affect the number of pulses picked by the AOM.

We achieve hyperspectral CARS using spectral focusing. ^{21,23}Figure 2a shows CARS spectra of DMSO and methanol (MeOH) in the C–H stretching region. To

determine the absolute sensitivity of our microscope for CARS, different concentrations of DMSO in deuterium oxide (D₂O) are measured by the hyperspectral CARS. A spectral phase retrieval method based on Kramers–Kronig relations is used to derive Raman spectra from chemical compounds using FCARS spectra. $^{36-38}$ The 2915 cm $^{-1}$ peak of DMSO diluted in D₂O is used to evaluate the CARS sensitivity. A plot of CARS signal intensity (proportional to $|\chi^{(3)}|^2$) versus DMSO concentration in D₂O (%) is shown in Figure 2b. A quadratic fitting shows signals and concentration satisfies eq 5. Larger

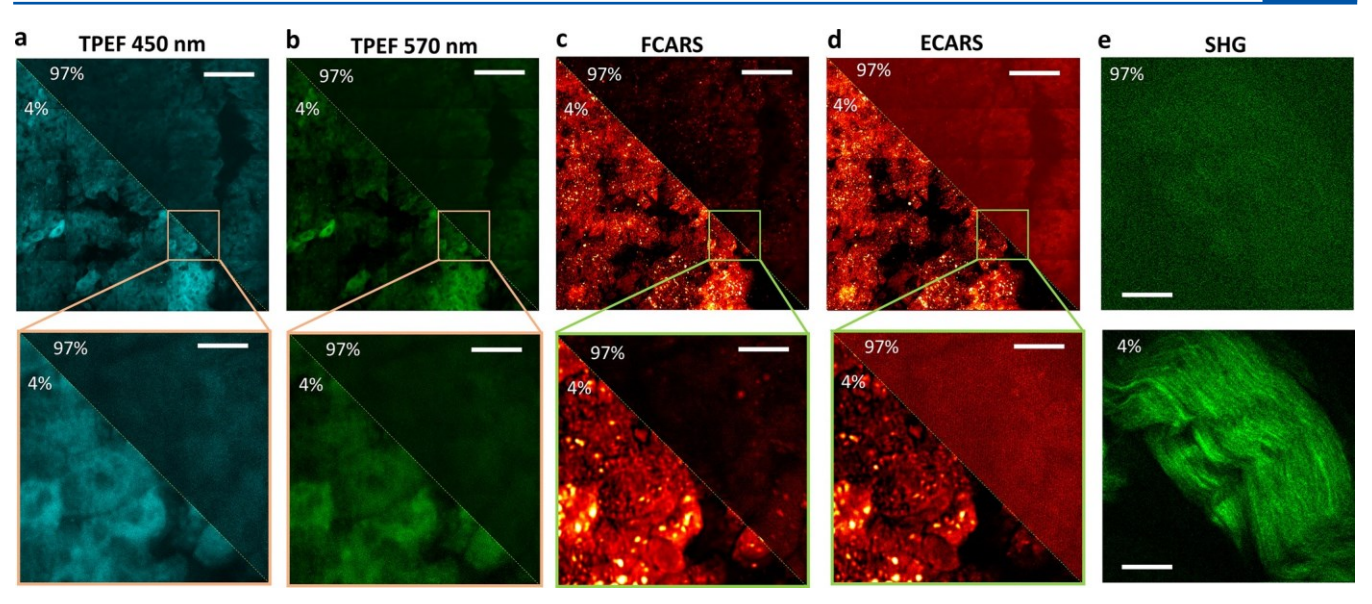


Figure 3. Pulse-picking nonlinear optical imaging of tissue samples. (a – d) Side-by-side comparison of 4 and 97% duty cycles with the same average input power for TPEF 450 nm (a), TPEF 570 nm (b), FCARS (c), and ECARS (d) imaging of a mouse liver sample (top) and the magnified selected region (bottom). (e) Side-by-side comparison of 97% (top) and 4% (bottom) duty cycles for SHG imaging of mouse tail tendon. Power at the samples: pump 18.0 mW, Stokes 12.6 mW for CARS and TPEF; 1.4 mW 1045 nm for SHG. Pixel dwell time: $10 \,\mu s$. Scale bars, 50 and $10 \,\mu m$ for top and bottom images, respectively, for panels (a – d), and $10 \,\mu m$ for panel (e).

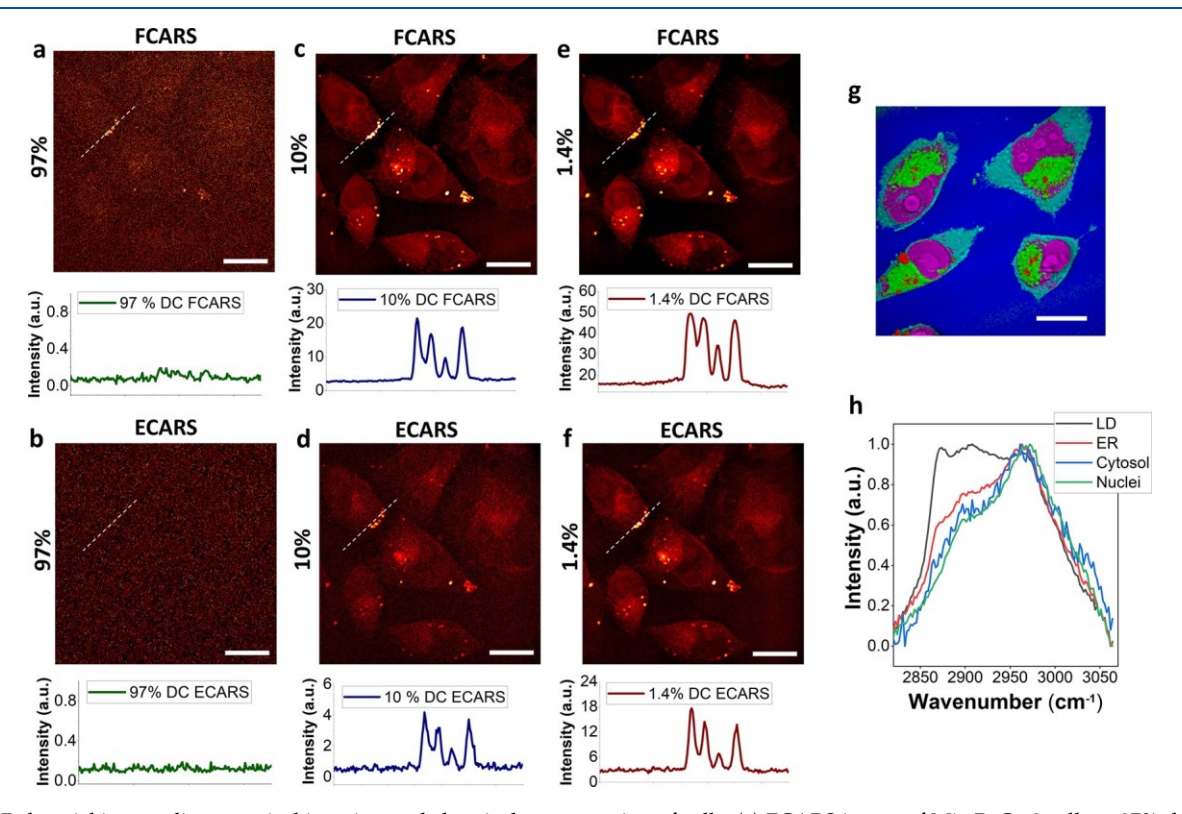


Figure 4. Pulse-picking nonlinear optical imaging and chemical segmentation of cells. (a) FCARS image of Mia PaCa-2 cells at 97% duty cycle (DC) with a 0.7 MHz modulation frequency (top panel) and the intensity plot along the dashed line (bottom panel). (b) ECARS image and intensity profile from the same field of view as in panel (a). (c-f) Similar FCARS or ECARS images and intensity profiles as in panels (a) and (b) acquired at 10 or 1.4% DC. (g) Chemical map of Mia PaCa-2 cells composed of the cytosol (cyan), endoplasmic reticulum (ER, green), nuclei (magenta), and lipid droplet (LD, red) compositions produced from spectral phasor unmixing. (h) Phase-retrieved Raman spectra from four cellular components. Scale bars, $10 \mu m$.

deviations at low concentrations are likely caused by noise from the nonresonant background. Spectrally retrieved Raman spectra (proportional to $\chi^{(3)}$) of DMSO below 1% concentration are shown in Figure 2c, which display a good linear

signal dependence on DMSO concentration. These results indicate that the lowest concentration detectable using 5.2 mW pump (478 W peak power), 6.2 mW Stokes (1076 W peak power) at the sample with 1.1 MHz modulation is between 0.1

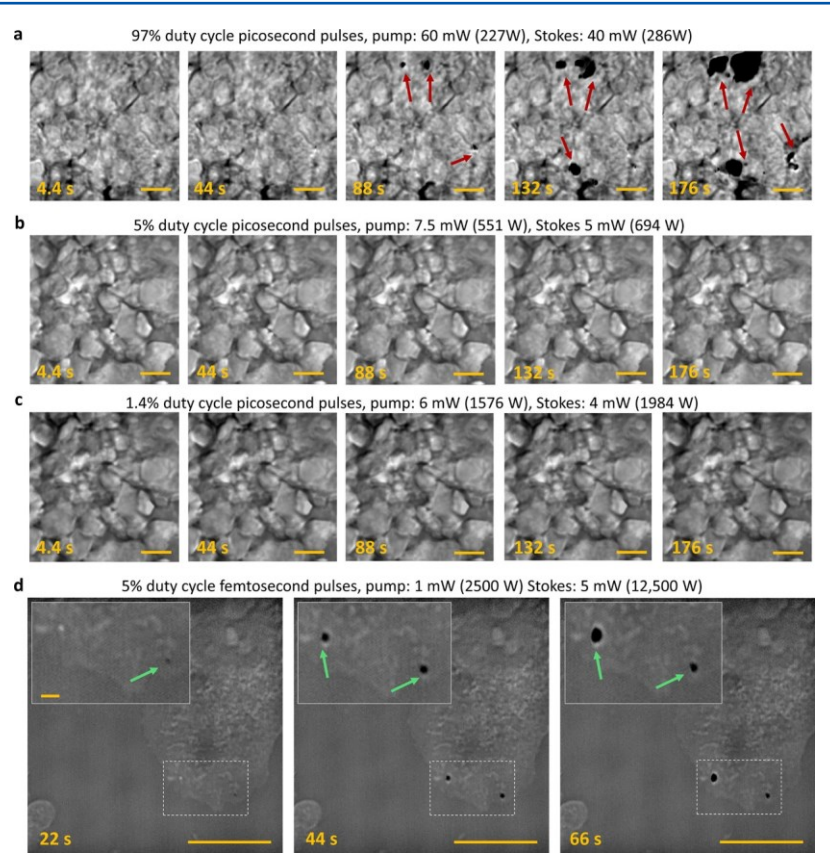


Figure 5. Evaluation of phototoxicity induced by different average power (6-100 mW) and peak power $(513-15\ 000\ \text{W})$ levels. (a-c) Time-lapse imaging of mouse spleen tissue slices at 97, 4, and 1.4% duty cycles, respectively. Average and peak power levels are adjusted to ensure the same CARS signal level. Red arrows point to the evolution of sample photodamage during imaging. (d) High peak power-induced photodamage for fixed Mia PaCa-2 pancreatic cancer cells. Pulse-picking of femtosecond laser pulses is applied in panel (d). Green arrows indicate multiphoton-absorption-induced photodamage. Pixel dwell time: $20\ \mu\text{s}$. Scale bars: $10\ \mu\text{m}$ for panels (a-d), $1\ \mu\text{m}$ for insets in panel (d).

and 0.5% DMSO. Using 0.7 MHz modulation with 2.0 mW pump (525 W peak power) and 3.7 mW Stokes (1835 W peak power) pulses, the DMSO symmetric stretching peak can be resolved for the 0.1% DMSO, corresponding to a concentration of 14 mM (Figure S3). By fitting the 2915 cm⁻¹ DMSO peak with a Lorentzian function, as shown in Figure 2d, we measure the spectral resolution of the CARS microscope to be 16.1 cm⁻¹ in the C–H region.

Figure 2e shows plots of retrieved Raman spectra of polystyrene (PS) and poly(methyl methacrylate) (PMMA) in the 1570–1750 cm⁻¹ Raman fingerprint region acquired using 1 μm PMMA and PS mixed particles. The PS peaks at 1583 (C�C stretching) and 1602 cm⁻¹ (ring-skeletal stretching) can be resolved, while the PMMA peak at 1736 cm⁻¹ is also detected. Using the strong peak at 1602 cm⁻¹, we measured a 9.1 cm⁻¹ CARS spectral resolution of our microscope in this region (Figure 2f). Figure 2g compares CARS images of mixed PMMA and PS beads at ~1602 cm⁻¹ using 97 and 4% duty cycles. A clear SNR and contrast improvement can be seen at the reduced duty cycle. By spectral phasor analysis of hyperspectral CARS images in the fingerprint region, we can separate PMMA and PS microparticles, as shown in Figure 2h.

Tissue and Cell Imaging by the Pulse-Picking Nonlinear Optical Microscope. To evaluate the sensitivity enhancement using the pulse-picking method for tissue imaging, we compare TPEF at 450 nm, TPEF at 570 nm, FCARS, and ECARS images of mouse liver tissue at 97 and 4% duty cycles under 1.1 MHz modulation (Figure 3a–d). CARS

excitation wavelengths are tuned to the CH₂ stretching at 2855 cm⁻¹. Signals in the TPEF 450 nm channel are majorly contributed by the autofluorescence from NADH, while those in the TPEF 570 nm channel are contributed by the autofluorescence from FAD. To better compare the contrast enhancement, we combine two duty cycle images into one and display half of each. We also select a smaller field of view and show a magnified image at the bottom of each large area image. These results show strong SNR enhancement for all modalities at a 4% duty cycle. We also show sensitivity enhancement of SHG imaging using mouse tail tendon in Figure 3e. Images from other tissue samples and at other modulation frequency/ duty cycles can be found in the Supporting Information (Figures S4-S8). These results highlight the potential of pulsepicking technology for better chemical imaging of intact biopsy samples for diagnostics.

Next, we apply pulse-picking CARS for cell imaging. Figure 4a—f compares single-color FCARS and ECARS images from Mia PaCa-2 cells at 97, 10, and 1.4% duty cycles, respectively. We use a 0.7 MHz modulation frequency and observe a continuous increase in signal and sensitivity for both FCARS and ECARS as the duty cycle decreases from 97 to 1.4%. To better compare the sensitivity improvement, we plot the intensity profiles along the lines in Figure 4a—f, which shows an SNR improvement of $\sim\!250\times$ at the 1.4% duty cycle. We note that the sensitivity enhancement for small lipid droplets (LDs) in the cells is less than the pure samples shown in Figure 1. This is due to the higher ratio of nonresonant contribution

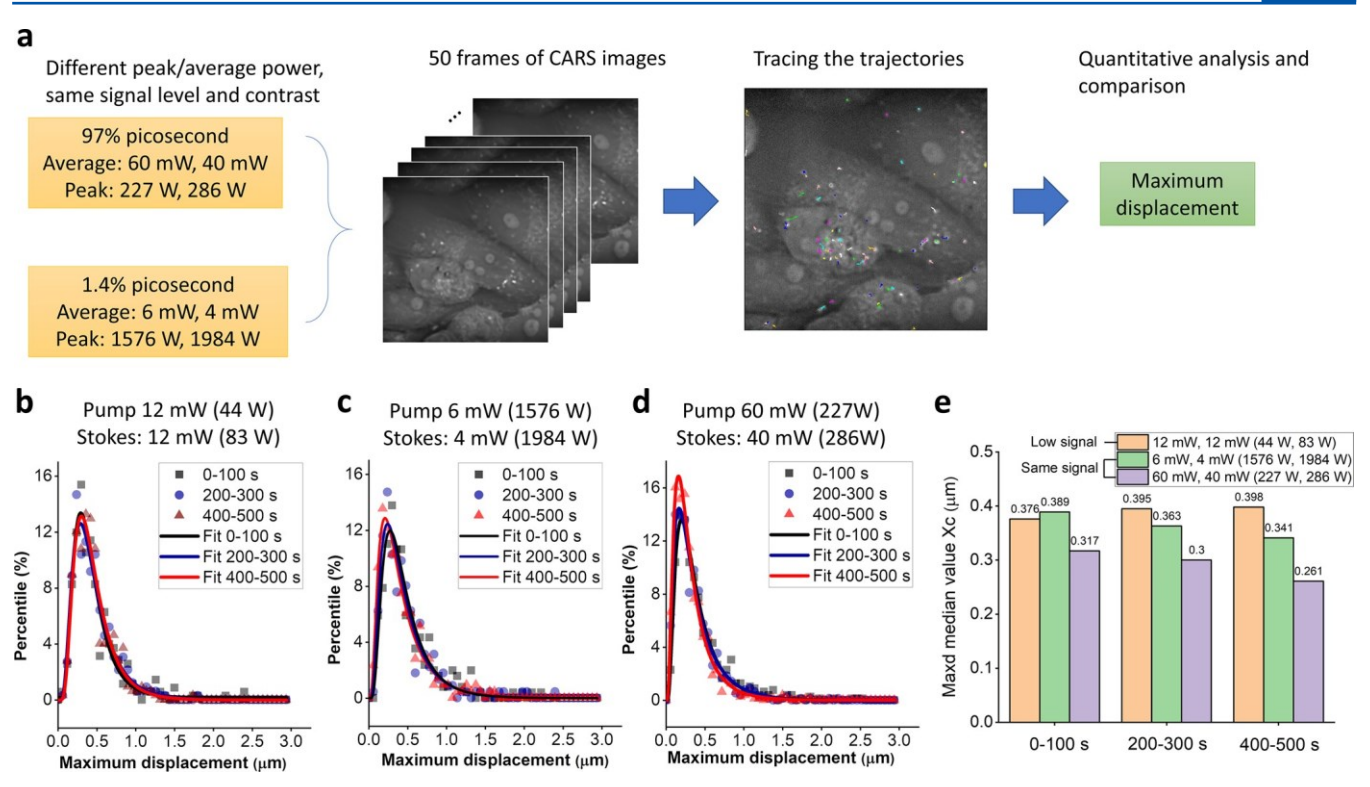


Figure 6. Quantification of LD intercellular dynamics for the evaluation of phototoxicity induced by different average (10-100 mW) and peak power (127-3560 W) levels. (a) Illustration of the workflow for CARS image stack acquisition, LD trajectory tracing, and quantitative analysis of the LD dynamics. Pixel dwell time: $10 \mu s$. (b) Histograms of LDs maximum displacement (μm) in HeLa cells using low average and peak power pulses. (c) Histograms of LD maximum displacement using low average power and high peak power pulses. (d) Histograms of LD maximum displacement using high average power and low peak power pulses. For panels (b-d), dots represent the experimental data from different time windows. Curves are lognormal fitting results. (e) Comparison of maximum displacement median values (x_c) of the lognormal fitting results in panels (b-d).

at the laser focus. Power at the sample for imaging is 10.8 mW (2836 W peak power) for the pump and 5.0 mW (2480 W peak power) for the Stokes. Cell imaging results using different duty cycles at 1.1 MHz modulation frequency are shown in Figure S9. We have also performed live-cell imaging of LDs and mitochondria using CARS and TPEF signals from a mitochondria marker. Images comparing 97, 10, and 4% duty cycles are shown in Figure S10. Hyperspectral CARS images of cells are performed using 2.0 mW pump and 3.7 mW Stokes average power at 10 µs pixel dwell time. By spectral focusing and spectral phasor unmixing, we can separate major cellular compositions, including cytosol, endoplasmic reticulum, nuclei, and LDs in cells using both FCARS and ECARS. The composited chemical map of cells and retrieved Raman spectra of four major components using FCARS are shown in Figure 4g,h, respectively. Composite chemical maps and individual cellular composition images for ECARS are shown in Figure S11. The separation capability of our hyperspectral CARS microscopy is comparable to spectral focusing-based hyperspectral SRS microscopy.^{23,39}

Photodamage of Tissue Samples at Different Average and Peak Power Levels. Finding the optimal laser average and peak power for label-free imaging is critical to ensuring the best sensitivity and minimum phototoxicity. Pulse-picking can significantly reduce thermally induced photodamage via single-photon absorption; however, at potential risk of increasing multiphoton-absorption-induced phototoxicity. 40,41 To evaluate and compare phototoxicity in different conditions, we maintain the same sensitivity and

image quality of CARS based on the curve shown in Figure 1g while using different average and peak power combinations by changing duty cycles. Figure 5a-c shows time-lapse CARS images of a mouse spleen section by decreasing the average power and increasing the peak power with a pixel dwell time of $20 \,\mu s$. At high average power and low peak power on the sample (Figure 5a), obvious photodamage is observed starting from 88 s of laser scanning. The damaged area continues to enlarge after longer laser exposure. However, at lower average power and higher peak power (Figure 5b,c), no detectable photodamage is observed. These results indicate that the laser pulses of ~12.5 mW combined average power and ~3600 W combined peak power are safe for mouse spleen imaging. Reducing the duty cycle to <5% of 80 MHz ps pulse trains can achieve such a power range for high sensitivity and low phototoxicity. To further increase the laser peak power, we bypass the chirping rods and apply the same method for picking fs laser pulses. As shown in Figure 5d, photodamage is detected at 44 s when the peak power of over 10 000 W is used in the Stokes beam despite the average power on the sample being very low. In Figure 5d, a fixed MIA PaCa-2 cell is used. The laser pulses are expected to induce more photodamage for the mouse spleen than for the cultured cells. Collectively, these results show that both the high average and high peak power of laser pulses can induce photodamage to biological samples. For nonlinear optical imaging, we believe that the combined average power of <12.5 mW and combined pulse peak power of <3600 W on the sample is safe for mouse spleen at 20 μ s pixel dwell time. This power is sufficient for CARS, TPEF, and

SHG imaging. The pulse-picking method enables optimal integration of hyperspectral CARS, TPEF, and SHG in a single imaging platform using chirped femtosecond (chirped to picosecond) laser pulses. Different tissue samples might have different power-safe ranges and can be evaluated similarly using the pulse-picking method. Other factors that might affect the photodamage are sample thickness, laser wavelength, pixel dwell time, and sample absorption properties. It is expected that samples with strong light absorbers such as pigments and heme would have lower peak and average power tolerance. Here, CARS images are used to visualize the overall sample morphology and photodamage due to the strong resonant and nonresonant signals generated from biological samples.

Lipid Droplet Dynamics for Quantification of Laser **Phototoxicity.** Measuring laser phototoxicity and lightinduced perturbation to cells is a challenging yet essential task for label-free imaging of live cells. Conventional ways rely on monitoring the cell shrinking or membrane blebbing to identify severe photodamage to cells.33,34 Cells showing these obvious structural and dynamic features are strongly perturbed and in the late stage of photo-induced apoptosis. In this work, we use intercellular dynamics to quantify photo-perturbation to live cells. Intercellular organelle dynamics are powered by ATP and therefore are more sensitive to probe and quantify perturbations to cells. It was shown that LD dynamics can be applied to quantify cell responses to temperature change and drug treatment. 42 In this work, we apply LD dynamics to evaluate photo-perturbation by laser pulses at different average and peak power ranges.

Figure 6a shows an illustration of the workflow used for data acquisition and analysis. We use the maximum displacement of LDs over the image acquisition time to evaluate photoperturbation to live HeLa cells. Fifty images are collected at 10 us per pixel (2 s per frame). The trajectory tracking of LDs is performed using a particle tracker ImageJ plugin.⁴³ A labwritten MATLAB code is used to perform quantitative and statistical data analysis.42,44 Histograms of LD maximum displacement at three time windows (0-100, 200-300, and 400-500 s) are plotted and compared in Figure 6b-d for different power ranges. We first measured a low average power (<24 mW total) and peak power (<130 W total) condition, which was shown to be safe for live-cell imaging⁴⁴ and shows almost no changes in LD dynamics over 500 s laser exposure. Next, we significantly increased the image contrast using pulsepicking and measured the low average power (<10 mW total) and high peak power (<3600 W total) condition (1.4% pulsepicking). The results in Figure 6c show very similar histogram profiles as in Figure 6b. Maintaining the same image contrast, we also compared the high average power (100 mW total) and low peak power (about 500 W total) conditions, which showed a significant decrease in the maximum displacement values starting from 1 to 100 s. This dynamic signature change is correlated with apoptosis and strong cellular perturbations.⁴² Longer exposure time continues to decrease the maximum displacement values, as shown in Figure 6d. To quantitatively compare the shifts of maximum displacement histograms, we fit the experimental data with lognormal functions and obtain the median values (x_c) as used in ref 42. Quantitative comparison of the x_c values shows that at the same imaging contrast, the high peak power condition used in this experiment gives less decrease in x_c compared to the high average condition, indicating less phototoxicity to live cells.

From these LD dynamic analyses, we believe that the total average power of <24 mW and the total peak power of <3600 W are safe conditions for live HeLa cell imaging for 500 s exposure. The safe and optimal power ranges for different cells might be different and are also relevant to the pixel dwell time, scanning range, and size of the focus. The pulse-picking method allows us to explore and achieve the best power range for different cells.

CONCLUSIONS

We developed a pulse-picking technology to increase the sensitivity of multimodal nonlinear optical imaging modalities, including hyperspectral CARS, TPEF, and SHG. Using function generator-controlled AOM and applying one of the excitation beams at a Bragg angle error condition, we collinearly combined both pump and Stokes beams at the 1st order of AOM. By reducing the duty cycle of the laser beams, we could improve the SNR of CARS, TPEF, and SHG sensitivity at low average input power. The pulse-picking technology gives better sensitivity enhancement for higher-order nonlinear optical processes.

Maintaining the peak power at a safe range, we showed that increasing the peak power gives better image contrasts and less phototoxicity. The photo-perturbation to biological systems is evaluated using intact mouse tissue sections and by quantification of LD dynamics in live cells. We show that reducing the duty cycle of 80 MHz can improve sensitivity and reduce phototoxicity. Our pulse-picking method can minimize the duty cycle to 1.4%, corresponding to a ~1 MHz repetition rate of ps lasers. We believe that the duty cycles of 1.4-5%, which correspond to 1-4 MHz repetition rates, are optimal for optical imaging using ps pulses. This finding is consistent with the previous report for single-color CARS imaging.³⁴ In this repetition rate range, the pulse peak power is below 1600 W for the pump and below 2000 W for the Stokes. These peak power values are within the typical range used for highrepetition-rate fs CARS imaging and multiphoton fluorescence microscopy. 14,18,31,45 Therefore, we conclude that the combined laser pulses below 24 mW average power and below 3600 W peak power at the sample are generally safe and optimal for nonlinear optical imaging of live cancer cells and tissue. These conditions can be achieved using low-repetition rate (e.g., 1–4 MHz) ps laser or high-repetition-rate (e.g., 80 MHz) fs laser pulses and can be flexibly controlled by the pulse-picking method.

The performance of pulse-picking nonlinear optical microscopes can be further improved in several ways. First, the efficiency of the AOM can be further improved using optimized crystal coating. Second, the decrease in sensitivity improvement for CARS at very low duty cycles is likely due to the pulse-picking variations and drifts caused by the unlocked phase between the laser repetition frequency and the modulation frequency, as well as the rise time difference between the pump and Stokes pulses. These variations only exist at the rise and fall time of each cycle and thus are not significant for high duty cycles. However, at very low duty cycles, since only a few pulses are picked, large deviations can be induced. Phase-locking the function generator to the laser repetition would further improve the sensitivity values at low duty cycles. Tighter focusing at the AOM can also further reduce the pulse-picking rise time.

Currently, the pulse-picking method is incompatible with SRS microscopy. Although the AOM produces the modulation

at a high frequency, SRS signals are overwhelmed by higher harmonic modulation frequency components of square waves. One possible approach for pulse-picking SRS is to modulate pump and Stokes beams separately at different frequencies and apply a sinusoidal wave for one of the beams.



ASSOCIATED CONTENT

Supporting Information

The Supporting Information is available free of charge at https://pubs.acs.org/doi/10.1021/acs.analchem.2c03284.

Supporting methods; calculation of the AOM rise time; CARS signal intensity as a function of pump or Stokes power; TPEF and SHG sensitivity enhancement at different modulation frequencies; sensitivity measurement using DMSO in D₂O; imaging of mouse tissue samples; cell imaging using 1.1 MHz modulation; livecell CARS and fluorescence imaging; and phasor spectral unmixing of epi-CARS imaging of cells; Figures S1–S11; and Table S1 (PDF)

AUTHOR INFORMATION

Corresponding Author

Chi Zhang — Department of Chemistry, Purdue University, West Lafayette, Indiana 47907, United States; Purdue Center for Cancer Research, West Lafayette, Indiana 47907, United States; Purdue Institute of Inflammation, Immunology, and Infectious Disease, West Lafayette, Indiana 47907, United States; orcid.org/0000-0002-7735-5614; Email: zhan2017@purdue.edu

Authors

Matthew G. Clark — Department of Chemistry, Purdue University, West Lafayette, Indiana 47907, United States Gil A. Gonzalez — Department of Chemistry, Purdue University, West Lafayette, Indiana 47907, United States

Complete contact information is available at: https://pubs.acs.org/10.1021/acs.analchem.2c03284

Author Contributions

C.Z. designed the project. M.G.C. and C.Z. designed and performed the experiments. M.G.C. and C.Z. analyzed the data. G.A.G. prepared cell and tissue samples. M.G.C. and C.Z. wrote the paper.

Notes

The authors declare no competing financial interest.

AC

ACKNOWLEDGMENTS

The authors want to thank Judy Hallett at Purdue University Bindley Bioscience Center for sharing the mouse carcass for tissue harvest. The authors also want to thank Dr. Garth Simpson for sharing the APE autocorrelator for the measurement of pulse width. The authors are grateful to the Center for Bioanalytical Metrology (CBM), an NSF Industry-University Cooperative Research Center, for providing funding for this project under NSF IIP 1916991, and to the members of the CBM Industry Advisory Board for valuable discussions and suggestions.



REFERENCES

(1) Xu, C.; Zipfel, W.; Shear, J. B.; Williams, R. M.; Webb, W. W. *Proc. Natl. Acad. Sci. U.S.A.* 1996, *93*, 10763–10768.

- (2) Huang, S.; Heikal, A. A.; Webb, W. W. *Biophys. J.* 2002, *82*, 2811–2825.
- (3) Campagnola, P. Anal. Chem. 2011, 83, 3224-3231.
- (4) Cox, G. Biophys. Rev. 2011, 3, 131.
- (5) Evans, C. L.; Xie, X. S. Annu. Rev. Anal. Chem. 2008, 1, 883–909.
- (6) Min, W.; Freudiger, C. W.; Lu, S.; Xie, X. S. *Annu. Rev. Phys. Chem.* 2011, *62*, 507–530.
- (7) Chung, C.-Y. J.; Potma, E. O. Annu. Rev. Phys. Chem. 2013, 64, 77–99.
- (8) Cheng, J.-X.; Xie, X. S. Science 2015, 350, No. eaaa8870.
- (9) Lombardini, A.; Mytskaniuk, V.; Sivankutty, S.; Andresen, E. R.; Chen, X.; Wenger, J.; Fabert, M.; Joly, N.; Louradour, F.; Kudlinski, A.; Rigneault, H. *Light: Sci. Appl.* 2018, 7, 10.
- (10) Huff, T. B.; Shi, Y.; Fu, Y.; Wang, H.; Cheng, J. X. *IEEE J. Sel. Top. Quantum Electron.* 2008, *14*, 4–9.
- (11) Chen, H.; Wang, H.; Slipchenko, M. N.; Jung, Y.; Shi, Y.; Zhu, J.; Buhman, K. K.; Cheng, J.-X. *Opt. Express* 2009, *17*, 1282–1290.
- (12) Meyer, T.; Baumgartl, M.; Gottschall, T.; Pascher, T.; Wuttig, A.; Matthäus, C.; Romeike, B. F. M.; Brehm, B. R.; Limpert, J.; Tünnermann, A.; Guntinas-Lichius, O.; Dietzek, B.; Schmitt, M.; Popp, J. *Analyst* 2013, *138*, 4048–4057.
- (13) Schwille, P.; Haupts, U.; Maiti, S.; Webb, W. W. Biophys. J. 1999, 77, 2251–2265.
- (14) Masters, B. R.; So, P. T. Opt. Express 2001, 8, 2–10.
- (15) Teng, S.-W.; Tan, H.-Y.; Peng, J.-L.; Lin, H.-H.; Kim, K. H.; Lo, W.; Sun, Y.; Lin, W.-C.; Lin, S.-J.; Jee, S.-H. *Invest. Ophthalmol. Vis. Sci.* 2006, 47, 1216–1224.
- (16) Tu, H.; Liu, Y.; Turchinovich, D.; Marjanovic, M.; Lyngsø, J. K.; Lægsgaard, J.; Chaney, E. J.; Zhao, Y.; You, S.; Wilson, W. L. *Nat. Photonics* 2016, *10*, 534–540.
- (17) van Huizen, L. M. G.; Radonic, T.; van Mourik, F.; Seinstra, D.; Dickhoff, C.; Daniels, J. M.; Bahce, I.; Annema, J. T.; Groot, M. L. *Trans. Biophotonics* 2020, *2*, No. e202000009.
- (18) Evans, C. L.; Potma, E. O.; Puoris'haag, M.; Côté, D.; Lin, C. P.; Xie, X. S. *Proc. Natl. Acad. Sci. U.S.A.* 2005, *102*, 16807–16812.
- (19) Légaré, F.; Evans, C. L.; Ganikhanov, F.; Xie, X. S. *Opt. Express* 2006, *14*, 4427–4432.
- (20) Kee, T. W.; Cicerone, M. T. Opt. Lett. 2004, 29, 2701–2703.
- (21) Hellerer, T.; Enejder, A. M. K.; Zumbusch, A. *Appl. Phys. Lett.* 2004, *85*, 25–27.
- (22) Knutsen, K. P.; Johnson, J. C.; Miller, A. E.; Petersen, P. B.; Saykally, R. J. Chem. Phys. Lett. 2004, 387, 436–441.
- (23) Fu, D.; Holtom, G.; Freudiger, C.; Zhang, X.; Xie, X. S. *J. Phys. Chem. B* 2013, *117*, 4634–4640.
- (24) Masia, F.; Glen, A.; Stephens, P.; Borri, P.; Langbein, W. *Anal. Chem.* 2013, *85*, 10820–10828.
- (25) Camp, C. H., Jr.; Lee, Y. J.; Heddleston, J. M.; Hartshorn, C. M.; Walker, A. R. H.; Rich, J. N.; Lathia, J. D.; Cicerone, M. T. *Nat. Photonics* 2014, *8*, 627–634.
- (26) Pegoraro, A. F.; Slepkov, A. D.; Ridsdale, A.; Moffatt, D. J.; Stolow, A. *J. Biophotonics* 2014, 7, 49–58.
- (27) Liao, C.-S.; Slipchenko, M. N.; Wang, P.; Li, J.; Lee, S.-Y.; Oglesbee, R. A.; Cheng, J.-X. *Light: Sci. Appl.* 2015, 4, e265.
- (28) Kano, H.; Segawa, H.; Okuno, M.; Leproux, P.; Couderc, V. J. Raman Spectrosc. 2016, 47, 116–123.
- (29) Chemnitz, M.; Baumgartl, M.; Meyer, T.; Jauregui, C.; Dietzek, B.; Popp, J.; Limpert, J.; Tünnermann, A. *Opt. Express* 2012, 20, 26583–26595.
- (30) Huland, D. M.; Charan, K.; Ouzounov, D. G.; Jones, J. S.; Nishimura, N.; Xu, C. *Biomed. Opt. Express* 2013, *4*, 652–658.
- (31) You, S.; Tu, H.; Chaney, E. J.; Sun, Y.; Zhao, Y.; Bower, A. J.; Liu, Y.-Z.; Marjanovic, M.; Sinha, S.; Pu, Y. *Nat. Commun.* 2018, *9*, No. 1.
- (32) Vernuccio, F.; Bresci, A.; Talone, B.; de la Cadena, A.; Ceconello, C.; Mantero, S.; Sobacchi, C.; Vanna, R.; Cerullo, G.; Polli, D. *Opt. Express* 2022, *30*, 30135–30148.
- (33) Nan, X.; Potma, E. O.; Xie, X. S. *Biophys. J.* 2006, *91*, 728–735. (34) Fu, Y.; Wang, H.; Shi, R.; Cheng, J.-X. *Opt. Express* 2006, *14*,
- (34) Fu, Y.; Wang, H.; Shi, R.; Cheng, J.-X. Opt. Express 2006, 14, 3942–3951.

Analytical Chemistry Article pubs.acs.org/ac

- (35) Le, T.; Langohr, I.; Locker, M.; Sturek, M.; Cheng, J.-X. J. Biomed. Opt. 2007, 12, No. 054007.
- (36) Vartiainen, E. M. J. Opt. Soc. Am. B 1992, 9, 1209–1214.
- (37) Liu, Y.; Lee, Y. J.; Cicerone, M. T. Opt. Lett. 2009, 34, 1363–
- (38) Hong, W.; Liao, C. S.; Zhao, H.; Younis, W.; Zhang, Y.; Seleem, M. N.; Cheng, J. X. ChemistrySelect 2016, 1, 513-517.
- (39) Huang, K.-C.; Li, J.; Zhang, C.; Tan, Y.; Cheng, J.-X. iScience 2020, 23, No. 100953.
- (40) Koester, H. J.; Baur, D.; Uhl, R.; Hell, S. W. Biophys. J. 1999, 77, 2226-2236.
- (41) Hopt, A.; Neher, E. Biophys. J. 2001, 80, 2029–2036.
- (42) Zhang, C.; Boppart, S. A. Anal. Chem. 2020, 92, 15943-15952.
- (43) Sbalzarini, I. F.; Koumoutsakos, P. J. Struct. Biol. 2005, 151, 182 - 195.
- (44) Zhang, C.; Li, J.; Lan, L.; Cheng, J.-X. Anal. Chem. 2017, 89, 4502 - 4507
- (45) Wang, H.; Fu, Y.; Zickmund, P.; Shi, R.; Cheng, J.-X. Biophys. J. 2005, 89, 581-591.

□ Recommended by ACS

3D Chemical Imaging by Fluorescence-detected Mid-**Infrared Photothermal Fourier Light Field Microscopy**

Danchen Jia, Ji-Xin Cheng, et al. MARCH 19, 2023 CHEMICAL & BIOMEDICAL IMAGING

READ **'**

Full-Spectrum CARS Microscopy of Cells and Tissues with **Ultrashort White-Light Continuum Pulses**

Federico Vernuccio, Dario Polli, et al. MAY 17, 2023

THE JOURNAL OF PHYSICAL CHEMISTRY B

READ C

Ultrafast Widefield Mid-Infrared Photothermal Heterodyne **Imaging**

Eduardo M. Paiva and Florian M. Schmidt

OCTOBER 05, 2022

ANALYTICAL CHEMISTRY

READ 2

Terahertz Nonlinear Ghost Imaging via Plane **Decomposition: Toward Near-Field Micro-Volumetry**

Luana Olivieri, Marco Peccianti, et al.

MARCH 10, 2023

ACS PHOTONICS

READ 2

Get More Suggestions >